Available online at www.sciencedirect.com
ScienceDirect
Journal of the Mechanics and Physics of Solids
54 (2006) 2474–2494

JOURNAL OF THE MECHANICS AND PHYSICS OF SOLIDS

www.elsevier.com/locate/jmps

Modeling the plastic response of thin metal membranes

S. Nemat-Nasser[a,*], A. Maximenko[b], E. Olevsky[b]

[a] *University of California, San Diego, 9500 Gilman Dr., La Jolla, CA 92093-0416 USA*
[b] *San Diego State University, 5500 Campanile Dr., San Diego CA 92182-1323 USA*

Received 1 March 2005; received in revised form 25 January 2006; accepted 17 April 2006

Abstract

Using a dislocations-based model of slip and crystal plasticity, we show by illustrative examples that the experimentally observed increase in the yield stress of very thin metallic membranes most likely is due to the variation of grain orientations through the thickness of the membrane, as well as the surface hardness due to oxidation or contamination, both of which generally are insignificant when there is a sufficient number of interior crystals through the membrane thickness; the overall effect may well be produced by a combination of these two causes. We show that crystal plasticity models can account for such size effects without a need for resorting to phenomenological strain-gradient models. We illustrate this using Nemat-Nasser's dislocations-based slip-induced crystal plasticity model that inherently includes length scales, although other rate-dependent slip models, e.g., the classical power-law slip model, most likely would qualitatively produce similar results. Our numerical results, based on the experimentally supported dislocation-induced slip model and the values of the model parameters given in Nemat-Nasser and Li [1998. Flow stress of F.C.C. polycrystals with application to OFHC Cu. Acta Mater. 46, 565–577], correlate well, both qualitatively and quantitatively, with the experimental results reported by Hommel and Kraft [2001. Deformation behavior of thin copper films on deformable substrates. Acta Mater. 49, 3935–3947] and Espinosa et al. [2004. Plasticity size effect in free-standing submicron polycrystalline FCC films subjected to pure tension. J. Mech. Phys. Solids 52, 667–689] for thin copper membranes, suggesting that, for submicron-sized samples, the classical crystal plasticity with slip models, does qualitatively account well for the small-size effects, and that quantitative predictions are obtained when, in addition, a physics-based dislocation model that includes length scales, is used. It is thus concluded that the length-scale effect and the size effect are two separate issues in metal plasticity, both of which

*Corresponding author. Tel.: +1 858 534 4914; fax: +1 858 534 2727.
E-mail address: sia@ucsd.edu (S. Nemat-Nasser).

0022-5096/$ - see front matter
doi:10.1016/j.jmps.2006.04.010

are nicely accounted for by physics-based dislocation models of crystal plasticity without a need to include the plastic strain gradient.

Keywords: Crystal plasticity; Polycrystalline material; Metallic membranes; Size effect

1. Introduction

The mechanical behavior of thin films is of importance in many modern applications. The miniaturization of structural and functional devices involves size reduction down to the single-crystal scale. The inelastic response of such thin metal films can be substantially different from that of their bulk counterparts; Choi and Suresh (2002). The flow stress of thin films, as a rule, exceeds that of the bulk material of the same composition and average grain size. This difference in mechanical response is usually viewed to be due to the substrate confinements. Recently, the uniaxial tensile response of metal membranes with submicron thickness has been studied experimentally by Hommel and Kraft (2001) and Espinosa et al. (2004). Hommel and Kraft observe that the flow stress and the hardening of thin copper films increase with decreasing film thickness and/or grain size, and are about two times higher in the (1 1 1)-grains compared to the (1 0 0)-grains; the measurements are made on the same polycrystalline film sample at various suitably oriented crystals. In a number of metallic samples considered by Espinosa and coworkers, considerable increase in the flow stress, essentially inversely proportional to the thickness of the membranes, has been observed.

Both phenomenological and dislocations-based models have been developed to explain this kind of phenomenon. Invoking the inherent dislocation-related microscopic length-scales in plasticity, several macroscopic strain-gradient plasticity models have been proposed to address this issue phenomenologically; Fleck et al. (1994), Fleck and Hutchinson (2001), and Hutchinson (2000). The introduction of the plastic strain gradient into the plasticity constitutive relations produces macroscopic length scales that can then be used as free parameters to fit the experimental results.

The sample-size effect and the dislocation-related microscopic length scales are two essentially distinct features of metal plasticity, as suggested by Nemat-Nasser (2004, p. 476). The strain-gradient plasticity theories combine these two effects into phenomenological length scales that emerge in the resulting constitutive relations. While the length scales are integral parts of a dislocation-based plasticity model, the sample-size effect is a problem-dependent issue that may or may not relate to the dislocation-based length scales. When the thickness of thin films is of the order of the constituting single crystals, the orientation of the crystals at which the measurements are made, the geometric and textural incompatibility between neighboring crystals, and the surface properties of the crystals (e.g., oxidation or contamination), most likely introduce constraints that may lead to substantially greater stiffness of the samples and also to a more brittle failure mode of otherwise very ductile metallic films. In cases of this kind, the interaction between individual crystals can be accounted for by direct application of crystal plasticity models; Cailletaud et al. (2003). The quantitative success of this kind of modeling to a great extent rests on the viability of the model used to represent the single-crystal behavior, although qualitative predictions by this approach would be successful even if one uses ad hoc slip models, e.g., a simple rate-dependent power law.

Calculations in the present article are based on a dislocation-based model proposed by Nemat-Nasser and Li (1998), Nemat-Nasser and Okinaka (1996), and Nemat-Nasser et al. (1998) for fcc crystals. Using the actual physics of metal plasticity, the model views the plastic deformation of fcc crystals to be due to slip on active $\{1\,1\,1\}$ slip planes and in the $\langle 1\,1\,0\rangle$ slip directions. Since the pioneering work of Orowan (1934), Polanyi (1934), and Taylor (1934), it is now generally known that such slip is induced by the motion of the mobile dislocations associated with the active slip systems; Havner (1992) and Nemat-Nasser (2004). This motion is resisted by short-range and long-range energy barriers that the dislocations must overcome through their thermal activation, assisted by the externally applied stresses; Kocks et al. (1975). The short-range barriers introduce temperature and rate dependence of the flow stress, and the long-range ones produce the work-hardening effects. Both contributions are associated with certain microscopic (actually, nanoscopic) length scales corresponding to the density of the associated dislocations, the nature of the short-range barriers, and the average size of the grains.[1]

For a typical slip system, the model is given, briefly discussed, and illustrated based on the experimental data for annealed and as-received oxygen-free high-conductivity (OFHC) copper presented by Nemat-Nasser and Li (1998). The physical parameters of this model for OFHC copper have been established by these authors through a series of careful experiments over a range of strain rates from 10^{-3} to 10^{4}/s and for temperatures from 77 to over 1000 K. Remarkably, the results for the annealed thin copper films presented by Hommel and Kraft (2001) are quantitatively simulated using the values of the constitutive parameters reported by Nemat-Nasser and Li (1998) for the annealed OHFC copper. In addition, the same model is used together with the data given by Nemat-Nasser and Li for the as-received OHFC copper, to examine the question of possible effects of the textural, geometric, and surface properties on the plastic response of the (un-annealed) thin metallic films used in Espinosa et al. (2004) experiments, arriving at remarkably good quantitative predictions. We also use a finite-element approach with our dislocation-based crystal-plasticity model to show through illustrative examples that the through-the-thickness textural and geometric incompatibility can also substantially affect the plastic response of a very thin film whose thickness is of the order of the size of a few crystals.

2. Kinematics of deformation of fcc crystal

The description of the kinematics of fcc crystal deformation follows the standard model; see, e.g., Nemat-Nasser (2004, Chapter 6 and references cited therein). The total deformation gradient, F, is divided into a non-plastic deformation gradient, F^*, and a plastic deformation gradient, F^p,

$$F = \left(\frac{\partial x}{\partial X}\right)^{\mathrm{T}}, \quad F = F^* F^p, \quad L = \dot{F}F^{-1}, \tag{1-3}$$

where X and x denote the reference and the current particle positions, respectively, and L is the velocity gradient, the superimposed dot standing for the time derivative, keeping the particle fixed. The non-plastic deformation gradient, F^*, includes the elastic deformation

[1]We note in passing that none of these microscopic (nano-scale) parameters seem to relate to the macroscopic plastic strain gradients, either directly or indirectly.

and the rigid body rotation. L is also divided into the non-plastic, L^*, and plastic, L^p, parts, and using Eq. (2) in (3), we have

$$L^* = \dot{F}^* F^{*-1}, \quad L^p = F^* \dot{F}^p F^{p-1} F^{*-1}. \tag{4,5}$$

The non-plastic deformation gradient can be decomposed as

$$F^* = V^e R^*, \quad V^e = 1 + \varepsilon, \tag{6,7}$$

where V^e is the left-stretch, expressed in terms of ε, the elastic strain measured in the rotated lattice, and R^* is the rigid-body rotation tensor. In general, the elastic strain, ε, is very small for most metals, being of the order of fractions of one percent. Therefore, the major part of the crystalline deformation is due to plastic deformation of the crystals, induced by plastic slip on various active slip systems. Since the overall crystal spin can be quite large, the non-plastic velocity gradient (4) is expressed as

$$L^* = \dot{\varepsilon} + \varepsilon\Omega^* - \Omega^*\varepsilon + \Omega^*, \quad \Omega^* = \dot{R}^* R^{*\mathrm{T}}, \tag{8,9}$$

where the higher order terms in ε are neglected, and Ω^* is the rigid-body spin. The symmetric and antisymmetric parts of L^* are the rates of the elastic lattice deformation, D^*, and lattice spin, W^*, respectively,

$$D^* = \dot{\varepsilon} + \varepsilon\Omega^* - \Omega^*\varepsilon, \quad W^* \simeq \Omega^*. \tag{10,11}$$

The plastic deformation is assumed to be solely due to crystalline slip. An fcc single crystal has four slip planes and three slip directions on each slip plane. As a result, the plastic part of the velocity gradient can be written as

$$L^{\mathrm{p}} = \sum_{\alpha=1}^{4} \sum_{a=1}^{3} \dot{\gamma}^{(\alpha a)} l^{(\alpha a)}, \quad l^{(\alpha a)} = R^* l_0^{(\alpha a)} R^{*\mathrm{T}}, \quad l_0^{(\alpha a)} = s_0^{(a)} \otimes n_0^{(\alpha)}, \tag{12-14}$$

where $\dot{\gamma}^{(\alpha a)}$ is the plastic slip rate on the slip plane α, in the slip direction a. Here, n_0 and s_0 are the unit normal of the slip plane and the unit vector in the slip direction, respectively. The zero subscript indicates initial configuration and the index (αa) stands for the ath slip direction on the αth slip plane. The symmetric, D^p, and antisymmetric, W^p, parts of L^p in Eq. (12) can be represented as

$$D^{\mathrm{p}} = \sum_{\alpha=1}^{4} \sum_{a=1}^{3} \dot{\gamma}^{(\alpha a)} p^{(\alpha a)}, \quad W^p = \sum_{\alpha=1}^{4} \sum_{a=1}^{3} \dot{\gamma}^{(\alpha a)} w^{(\alpha a)}, \tag{15,16}$$

$$p^{(\alpha a)} = R^* p_0^{(\alpha a)} R^{*\mathrm{T}}, \quad w^{(\alpha a)} = R^* w_0^{(\alpha a)} R^{*\mathrm{T}}, \tag{17,18}$$

$$p_0^{(\alpha a)} = \frac{1}{2}(l_0^{(\alpha a)} + l_0^{(\alpha a)\mathrm{T}}), \quad w_0^{(\alpha a)} = \frac{1}{2}(l_0^{(\alpha a)} - l_0^{(\alpha a)\mathrm{T}}). \tag{19,20}$$

The symmetric, D, and the antisymmetric, W, parts of the total velocity gradient are now given by

$$D = D^* + D^p, \quad W = W^* + W^p. \tag{21,22}$$

The important feature of relation (15) is that among twelve tensors, $p^{(\alpha a)}$, only five are linearly independent. There are seven additional relations between these tensors. As shown by Nemat-Nasser and Okinaka (1996), these relations are

$$p^{(\alpha 1)} + p^{(\alpha 2)} + p^{(\alpha 3)} = 0, \quad \alpha = 1, \ldots 4, \tag{23}$$

$$-p^{(11)} + p^{(12)} + p^{(43)} = 0, \quad -p^{(12)} - p^{(33)} + p^{(41)} = 0, \quad p^{(13)} - p^{(21)} + p^{(32)} = 0. \tag{24-26}$$

With the aid of these relations, all slip rates can be computed unambiguously using rate-dependent slip models.

3. Constitutive relations for single fcc crystal

Since the lattice elastic distortion is very small, we assume that the Jaumann rate, $\overset{\nabla}{\sigma}$, of the Cauchy stress tensor, σ, is linearly related to the lattice elastic deformation rate,

$$\overset{\nabla}{\sigma} = C^* : D^*, \quad \overset{\nabla}{\sigma} = \dot{\sigma} + \sigma\Omega^* - \Omega^*\sigma, \tag{27,28}$$

where C^* is the elasticity tensor in the rotated lattice. In modeling the Hommel–Kraft and Espinosa et al. results, we use the measured shear modulus reported by these authors. For the illustrative examples, we assumed isotropic elasticity. In all cases, we take the Poisson's ratio to be 0.34 (for copper).

The resolved shear stress, $\tau^{(\alpha a)}$, acting on the αath slip system is expressed in terms of the slip rate, temperature, and the accumulated crystal slip, by (Nemat-Nasser et al., 1998)

$$\tau^{(\alpha a)} = \tau_0 \left\{ 1 - \left(-\frac{kT}{G_0} \left(\ln \frac{\dot{\gamma}^{(\alpha a)}}{\dot{\gamma}_0} + \ln f(\gamma, T) \right) \right)^{1/q} \right\}^{1/p} f(\gamma, T) + \tau_a^{00} + \tau_a^0 g(\gamma), \tag{29}$$

where T is the temperature, and the resolved shear stress associated with the αath slip system is given by the following inner product of σ and $p^{(\alpha a)}$:

$$\tau^{(\alpha a)} = \langle \sigma, p^{(\alpha a)} \rangle. \tag{30}$$

We have discussed the derivation of Eq. (29) in what follows.

Note in passing that, in view of this, Eqs. (23)–(26) take on the following alternative form:

$$\tau^{(\alpha 1)} + \tau^{(\alpha 2)} + \tau^{(\alpha 3)} = 0, \quad \alpha = 1, \ldots, 4$$
$$-\tau^{(11)} + \tau^{(12)} + \tau^{(43)} = 0, \quad -\tau^{(12)} - \tau^{(33)} + \tau^{(41)} = 0, \quad \tau^{(13)} - \tau^{(21)} + \tau^{(32)} = 0. \tag{31-34}$$

In Eq. (29), the functions f and g characterize the density of dislocations that intersect the slip plane and the total dislocation density, respectively. The parameter γ is the accumulated effective plastic strain of the crystal, used here as an (independent) internal

("time") parameter to measure the internal structural changes, being a non-decreasing quantity; it is given by

$$\gamma = \sum_{\alpha=1}^{4}\sum_{a=1}^{3}\int_0^t \left|\dot{\gamma}^{(\alpha a)}(\xi)\right| \mathrm{d}\xi. \tag{35}$$

Expression (29) is based on the dislocation-model developed by Nemat-Nasser and Li (1998) to represent the experimental data they produced for OFHC copper over the range of strain rates from 10^{-3} to 10^{4}/s and temperatures from 77 to over 1000 K, using an Instron testing machine and special recovery Hopkinson techniques; see Nemat-Nasser et al. (1991), and Nemat-Nasser and Isaacs (1997). In this approach, one starts with Orowan's expression, $\dot{\gamma} = b\rho_m v$, where b is the magnitude of the Burgers vector, ρ_m is the density of the mobile dislocations, and v is their average velocity. This velocity is expressed by $v = \ell_s \omega$, where ℓ_s is the average dislocation spacing, and ω is the frequency at which the dislocations overcome their short-range energy barriers. If the barrier energy per unit dislocation length is ΔG, then it can be shown that

$$\omega = \omega_0 \exp\{-\Delta G/kT\}. \tag{36}$$

This is obtained by minimizing the free energy, $\Phi = \omega\Delta G - TS$, with respect to ω, where $S = k\ \ln(\omega_0!/(\omega_0-\omega)!\omega!)$ is the configurational entropy, noting that $\omega_0 \gg \omega \gg 1$, and using Sterling's approximation for the logarithm of the factorial of large numbers. For the fcc metals, the dislocations that intersect the slip planes are the primary barriers to the motion of the mobile dislocations that glide on these planes. Thus, the average spacing of the barriers is given by $\ell_s = \rho^{-1/2}$, where ρ is the average density of the dislocations. It has been suggested by Ono (1968) and Kocks et al. (1975) that ΔG can be expressed by

$$\Delta G = G_0\left[1 - \left(\frac{\tau - \tau_a}{\hat{\tau}}\right)^p\right]^q, \tag{37}$$

where τ_a is the shear stress due to the elastic field of all dislocations, grain boundaries, and other defects, G_0 is the total barrier energy per unit dislocation length, $\hat{\tau}$ is the shear stress required for the dislocations to overcome their barriers without the assistance of their thermal energy, and p and q are constants that characterize the barrier profile. Ono (1968) has shown that, for many cases, $0 < p \leqslant 1$ and $1 \leqslant q \leqslant 2$. Nemat-Nasser and coworkers have verified this for many refractory and other metals; see Nemat-Nasser (2004, pp. 235 and 238). For copper, $p = 2/3$ and $q = 2$, have been experimentally established in Nemat-Nasser and Li (1998). In addition, experimental results show that the athermal part of the flow stress can be represented as

$$\tau_a = \tau_a^{00} + \tau_a^0 \hat{g}(\rho). \tag{38}$$

Putting the above results together, the flow stress finally becomes

$$\tau = \hat{\tau}_0\left\{1 - \left(-\frac{kT}{G_0}\left(\ln\frac{\dot{\gamma}}{\dot{\gamma}_0} + \ln\frac{\ell_0}{\ell_s}\right)\right)^{1/q}\right\}^{1/p}\frac{\ell_0}{\ell_s} + \tau_a^{00} + \tau_a^0\hat{g}(\rho),$$
$$\hat{\tau}_0 = \frac{G_0}{b\lambda\ell_0}, \quad \dot{\gamma}_0 = b\rho_m\omega_0\ell_0, \tag{39}$$

where ℓ_0 is some reference average length scale, e.g., the average dislocation spacing of the annealed metal, and λ is the width of the energy barrier.

Now, to simplify the above relation for the present application, we use the accumulated total plastic slip, γ, as a time parameter, and assume that ℓ_s/ℓ_0 changes with this accumulated plastic slip and temperature, T, while the athermal part, $\hat{g}(\rho)$, varies with γ only. In other words, we use a simple constitutive model to express the dislocation density associated with ℓ_s in terms of γ and T, say, $\ell_0/\ell_s = f(\gamma, T)$, and set $\hat{g}(\rho) = g(\gamma)$. In this manner we reduce Eq. (38) to (29).

To specify the functions $f(\gamma, T)$ and $g(\gamma)$ in Eq. (29), note that $f(\gamma, T)$ must be an increasing function of γ and a decreasing function of T, while $g(\gamma)$ must increase with γ. Experimental data suggest that these functions may be approximated as follows:

$$f(\gamma, T) = 1 + a_0(1 - (T/T_m)^2)\gamma^{1/2}, \quad g(\gamma) = \gamma^{n_1}, \tag{40}$$

where $T_m = 1357\,\mathrm{K}$ is the melting temperature for copper, and the values of the other constitutive parameters are given in Table 1 for both annealed and as-received OFHC copper, taken from Nemat-Nasser and Li (1998). Figs. 1 and 2, taken from Nemat-Nasser and Li (1998), compare the model predictions with the experimental results for the annealed case, and Figs. 3 and 4 are for the as-received case, respectively. Also, it has been shown by Kapoor and Nemat-Nasser (1998) for many different metals that, at high strain

Table 1
Material parameters, from Nemat-Nasser and Li (1998)

Parameter	p	q	k/G_0 (10^{-5}/K)	$\dot{\gamma}_0$ (10^{10}/s)	τ_0 (Mpa)	a_0	n_0	τ_a^0 (Mpa)	n_1
Annealed	2/3	2	4.9	2	46	20	1/2	220	0.3
As-received	2/3	2	4.9	2	400	1.8	1/2	220	0.3

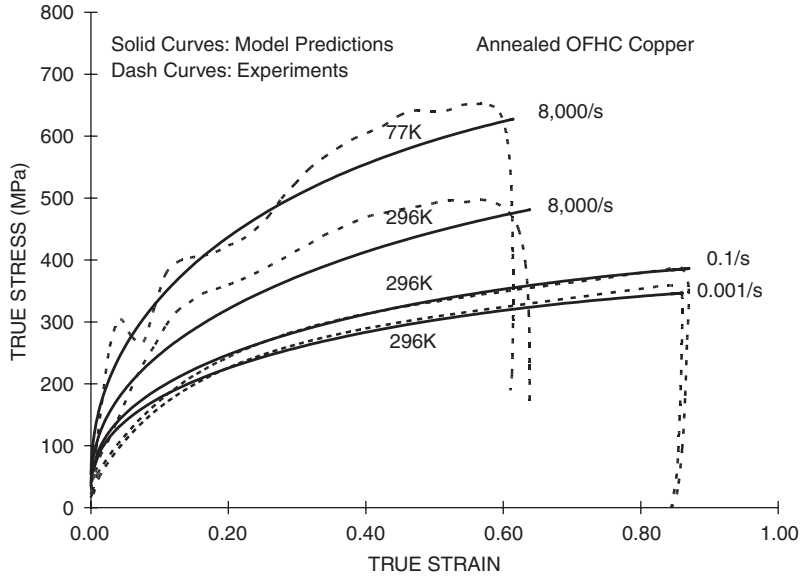

Fig. 1. Comparison between the model predictions and the experimental results for annealed OFHC copper at indicated initial temperatures and strain rates.

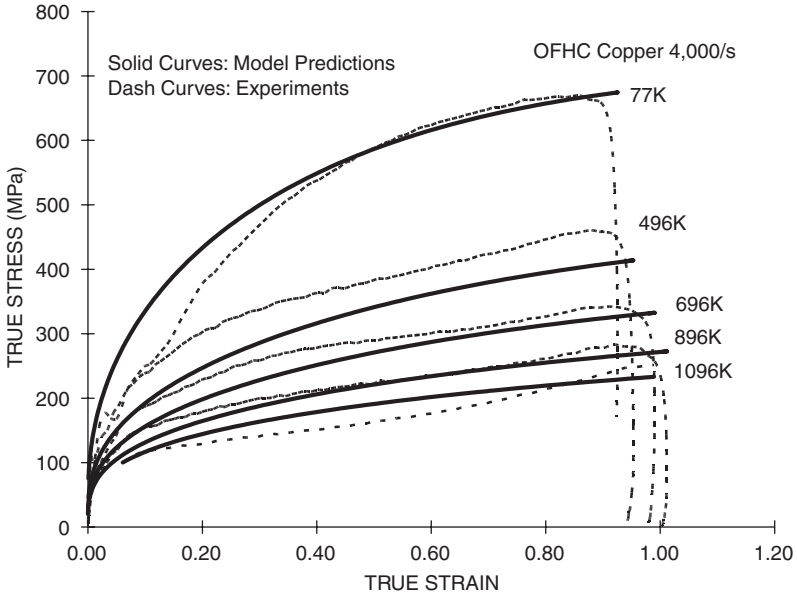

Fig. 2. Comparison between the model predictions and the experimental results for annealed OFHC copper at indicated initial temperatures and 4000/s strain rate.

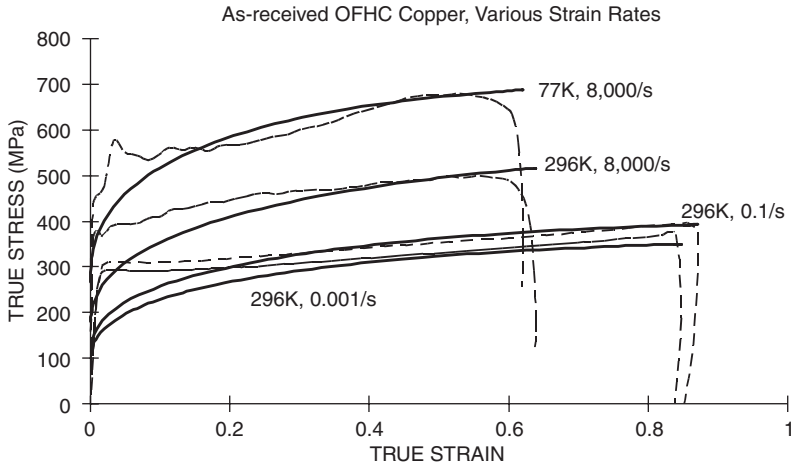

Fig. 3. Comparison between the model predictions and the experimental results for annealed OFHC copper at indicated initial temperatures and strain rates.

rates and for suitably large strains, essentially all the stress work is converted into heat, with the stored elastic energy of the dislocations being negligibly small. On the other hand, when metals are deformed plastically by only a few percent strain, some of the stress work is stored in the material in the form of the elastic energy of the dislocations. Stroh (1953) has calculated this to be about 4–5% of the total stress work, at small strains. Therefore, in

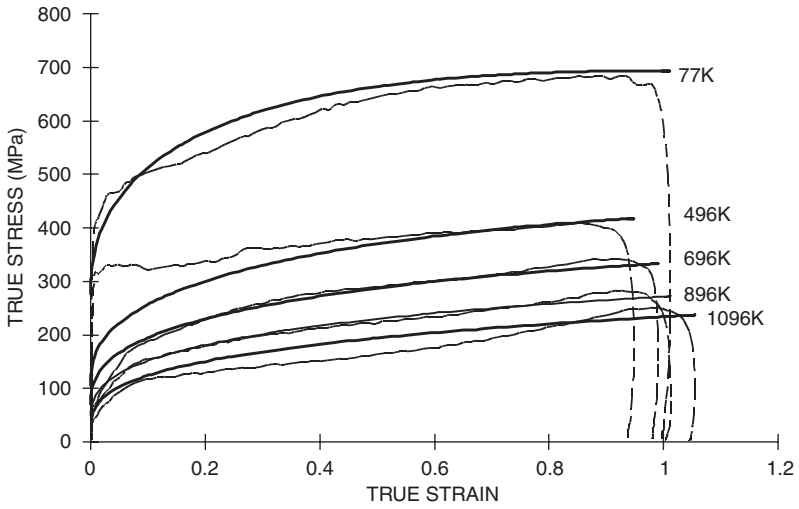

Fig. 4. Comparison between the model predictions and the experimental results for annealed OFHC copper at indicated initial temperatures and 4000/s strain rate.

Figs. 1–4, the temperature change due to plastic work is taken into account in calculating the temperature, T, assuming that all the stress work is used to heat the sample, whereas in the next section where only a few percent strains are involved, 95% of the stress work is assumed to be lost into heat.

As is seen from Figs. 1 to 4, the model has good predictive capability for temperatures from 77 to 1096 K and strain rates from 10^{-3} to 8000/s. As is also seen, except for τ_0 and a_0, all other constitutive parameters are the same for the annealed and as-received material in this case. Since the density of dislocations in an as-received copper is about two orders of magnitude greater than that in an annealed copper, we expect that τ_0 should be an order of magnitude greater in the former case relative to the latter. For the same reason, it is expected that a_0 should change by an order of magnitude when an as-received sample is annealed. The values of these parameters in Table 1 clearly accord with these observations.

4. Numerical modeling of deformation of polycrystals

In the classical theory of crystal plasticity, as originated in 1934 from the contributions of Orowan, Polanyi, and Taylor, the slip rate of each slip system of a given crystal is assumed to vary only in time with loading but not within the crystal itself, so that for each crystal the velocity gradient (12) is a function of time only. Different crystals in a polycrystalline solid, however, in general will have different velocity gradients, depending on their orientation, size, and other factors. We therefore may treat each crystal as an element in a finite-element modeling, and examine the effects of the textural incompatibilities on the overall response of the polycrystal. Since, in the present application, we are concerned with only a few percent plastic strains of thin membranes, the resulting numerical results should adequately capture the essence of the problem.

The numerical modeling may be based on the virtual work-rate principle, according to which the required stress equilibrium is expressed by

$$\Phi = \int_V \langle \sigma, \delta D \rangle \, \mathrm{d}V = 0, \tag{41}$$

where V is the volume of the considered body and the symbol δD denotes variation of the strain-rate tensor. Relation (41) and the boundary conditions provide all necessary equations for the prediction of the polycrystal deformation. In our modeling, we considered only kinematical boundary conditions with velocities specified over certain parts of the boundary of the polycrystal, the rest of the boundary being traction-free. In view of Eq. (21), Eq. (41) can be rewritten as

$$\Phi = \Phi^p + \Phi^{\mathrm{e}}, \quad \Phi^p = \int_V \langle \sigma, \delta D^p \rangle \, \mathrm{d}V, \quad \Phi^{\mathrm{e}} = \int_V \langle \sigma, \delta D^* \rangle \, \mathrm{d}V. \tag{42-44}$$

In Φ^{e}, we replace the stress tensor by

$$\sigma = \sigma_{t-\Delta t} + \dot{\sigma}\Delta t = \sigma_{t-\Delta t} + (C^* : D^* - \sigma\Omega^* + \Omega^*\sigma)\Delta t, \tag{45}$$

where t is the current time and Δt is the time increment. In this incremental approach, we assume that the stress and strain fields at $t - \Delta t$ are known, and then seek to extrapolate to obtain their values at t. Thus, in Eq. (45), $\sigma_{t-\Delta t}$ is known and σ, D^*, and Ω^* are to be evaluated at t.

The term Φ^p is the work-rate of plastic deformation that can be assessed in two ways. The first approach is to follow Nemat-Nasser and Okinaka (1996). This is discussed below, and the second approach, which consists of a direct application of a finite-element method, is discussed in Section 8. For the first alternative, we start by taking the inner product of D^{p} and $p^{(\alpha a)}$, to arrive at the following set of equations:

$$\left\langle D^p, p^{(\alpha a)} \right\rangle = \sum_{\beta=1}^{4} \sum_{b=1}^{3} \dot{\gamma}^{(\beta b)} H^{(\alpha a)}_{(\beta b)}, \quad H^{(\alpha a)}_{(\beta b)} = \left\langle p^{(\alpha a)}, p^{(\beta b)} \right\rangle. \tag{46,47}$$

The set Eq. (46) consists of 12 equations, but, in view of Eq. (23)–(26), only five of these are independent. Using Eqs. (31)–(34), we obtain seven additional relations among 12 slip rates, $\dot{\gamma}^{(\alpha a)}$, and hence, noting plastic incompressibility, we can calculate all 12 slip rates,

$$\dot{\gamma}^{(\alpha a)} = \sum_{i=1}^{5} A^i_{(\alpha a)} \left\langle D^p, p^{(i)} \right\rangle, \tag{48}$$

where $p^{(i)}$ denotes the selected five independent slip systems, with $A^i_{(\alpha a)}$ being the known coefficients. Upon substitution of Eq. (48) into Eq. (29) we obtain a set of non-linear equations that relate the resolved shear stresses to the components of the plastic strain-rate tensor,

$$\tau^{(\alpha a)} = F\left(\left\langle D^p, p^{(i)} \right\rangle\right), \tag{49}$$

where F is a non-linear function corresponding to Eq. (29). The plastic work-rate, Φ^p, is given by

$$\Phi^p = \sum_{\alpha=1}^{4} \sum_{a=1}^{3} \int_V \tau^{(\alpha a)} \delta\dot{\gamma}^{(\alpha a)} \, \mathrm{d}V. \tag{50}$$

This work-rate is now expressed in terms of the strain-rate tensor D^p by substituting Eqs. (48) and (49) into Eq. (50). The actual computations are performed using the method of plastic-predictor/elastic-corrector developed by Nemat-Nasser and coworkers, which is efficient, accurate, and stable; for a detailed discussion, illustrative examples, and references, see Nemat-Nasser (2004, Chapter 5). The application of the method to crystal plasticity has been made by Nemat-Nasser and Okinaka (1996) and to frictional granular materials with dilatancy and pressure sensitivity by Balendran and Nemat-Nasser (1993a, b). As will be illustrated in Section 6, with this method all active slip systems are unambiguously calculated for the rate-dependent models; for the details of the computational algorithm that have been used in crystal plasticity, see Nemat-Nasser (2004, Subsection 6.5.11, p. 462).

5. Application to thin-film data

We now first apply the model to predict the results reported by Hommel and Kraft (2001), using the values of the model parameters given in Table 1 for the annealed case (first row). Then we consider the corresponding data presented by Espinosa et al. (2004) for un-annealed thin copper membranes, and use the model parameters for the as-received case (second row) of Table 1.

Hommel and Kraft (2001) report the results of uniaxial tension of thin copper films, deposited on a 250 μm thick Ni sheet coated with a thin layer of polyimide, and annealed at 200 °C for 60 min. *The macroscopic strain is measured directly optically, and the axial stress is obtained for the* (1 1 1)- *and* (1 0 0)-*grain orientations, using* X-ray *measurements of the changes in the corresponding lattice dimensions and Hooke's law.* The Ni substrate is used to prevent the compression of the samples upon unloading. This unloading is necessary for the X-ray measurements. The reported effective strain rate is about 10^{-7}/s. The (1 1 1)- and (1 0 0)-grains are oriented with their [2 1 1] and [0 0 1] directions along the loading axis, respectively. From the measured data, and using a Poisson ratio of 0.34, the elastic shear moduli of 44 and 16.4 GPa are inferred from these authors' results. Fig. 5 shows the experimental data, extracted from Fig. 2(a) of Hommel and Kraft (2001, p. 3940). While the (1 0 0)-data start with zero stress at zero strain, the (1 1 1)-data start with about 35 MPa stress at (reported) zero strain. Hence, the two sets of data do not have a common origin.

Using the parameter values given in Table 1 for the annealed copper (first row), a strain rate of 10^{-7}/s, and $T = 296$ K, we have calculated the effective stress for two cases, one corresponding to grains that are oriented in the (1 1 1)-plane with their $[\bar{2}\,1\,1]$ axis along the loading direction, and the other for (1 0 0) grains with their [0 0 1] axis in the loading direction. Noting the difference in the origin of the two data sets, the results are shown in Fig. 5 by solid curves. The reader should note that no adjustment has been made in the values of the parameters that Nemat-Nasser and Li (1998) have reported for OFHC copper, based on their set of macroscopic experiments. Here, we have simply used those reported values of the parameters and crystal plasticity, as detailed by Nemat-Nasser (2004, Chapter 6), to obtain the results presented in Fig. 5.

We now examine the data presented in Espinosa et al. (2004) for un-annealed thin and thick copper films. These authors report experimental results of uniaxial tension of metal membranes with submicron to micron thicknesses. Unlike the data in uniaxial extension of thin copper wires reported by Fleck et al. (1994), Espinosa et al. observe that the uniaxial deformation of the membranes strongly depends on the thickness, with the uniaxial tensile

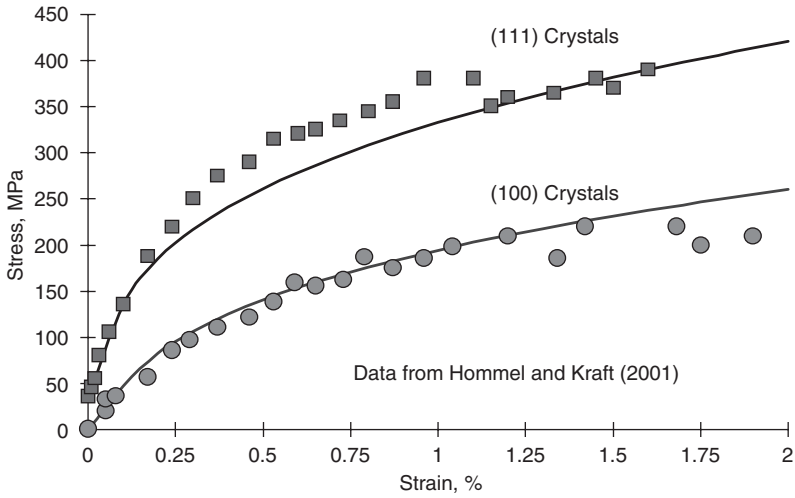

Fig. 5. Locally measured stress in crystals with $[\bar{2}\,1\,1]$ (upper data points) and [0 0 1] (lower data points) in the loading direction vs. optically measured overall macroscopic strain of a polycrystalline membrane and simulation results using the values of the model parameters reported by Nemat-Nasser and Li (1998) for annealed OFHC copper (Table 1, first row).

yield limit increasing as the membrane thickness decreases. This effect is observed only for samples with submicron thicknesses, i.e., when the thickness is of the order of the size of one or two crystals in the polycrystalline membranes.

Membranes of three different metals have been investigated, namely gold, copper, and aluminum. It has been found for aluminum that the samples essentially lose their plasticity when shaped into a membrane with a thickness of the order of the size of a couple of grains. It is known that aluminum films are usually covered by a thin layer of strong, adherent native oxide that generally is under an in-plane compression. Surface crystals that bear such an oxide layer have greater stiffness and resistance to plastic deformation than do the bulk crystals; i.e., these surface crystals do not deform plastically until their surface oxide layer is fractured. As a result, the yield limit of the surface layer crystals is expected to be greater than that of the interior grains, rendering the membrane plasticity to be dependent on the thickness of the crystals within the oxidized surface layer as compared with the overall membrane thickness. In Sections 7 and 8, we consider a finite-element model that allows examining the through the thickness textural incompatibility in membranes that are only a few grains thick.

Here, we use our crystal-plasticity model together with the data for the un-annealed copper (Table 1, second row) to check how well the model can predict the results presented in Fig. 7(b) of Espinosa et al. (2004, p. 680). Again, we do not make any adjustments to the values of the parameters that are reported by Nemat-Nasser and Li (1998) for their as-received OFHC copper results.

In their Figs. 7(a) and (b), Espinosa et al. (2004) show that, while the membranes of width 5, 10, and 20 μm display similar stress–strain relations, a change in thickness from 1.0 to 0.2 μm results in a substantial increase in the flow stress. For an average grain size of about 100 nm, there are no more than two grains through the thickness of the thin membranes, while for the 1.0 μm membranes there may be 5–10 grains per thickness. Also,

the sample preparation suggests possible grain contamination which can affect the 0.2 nm membranes but not noticeably the 1.0 μm membranes. In addition, the grain orientations through the thickness are most likely distributed over a wide range for the thick membranes, whereas in the case of thin membranes, most grains would have their (1 1 1)-plane parallel to the membrane surface, as commented on by Espinosa and coworkers. Another fact is the strain rate which varies in a given experiment with the membrane length; although the authors comment that the strain rate remains in the range of 10^{-5}/s. Since the model results are also affected by the strain rate, in what follows, the results are given for three strain rates 10^{-4}, 10^{-5}, and 10^{-6}/s, which are expected to cover the rates that a sample may have experienced.[2]

Based on the above observations, we allow for the variation in the orientation for the grains of the thick membrane but assume a common orientation for the grains in the thin membrane. We set $\tau_a^{00} = 0$, 75 MPa for the thick and thin membranes, respectively. The second value takes into account potential surface contaminations, as well as the initial single-crystal slip resistance reported by Wu et al. (1991). From Fig. 3, it is also seen that the as-received samples show a pronounced initial yield stress at room temperature and low strain rates, much higher than that observed in the corresponding curves for the annealed samples in Fig. 1. We use a shear modulus of 46.6 GPa (obtained using the Young modulus of 125 GPa, as reported by Espinosa et al., and a Poisson ratio of 0.34) for both cases, and present results for three strain rates, namely 10^{-4}, 10^{-5}, and 10^{-6}/s. For the thick membrane, we use a Taylor averaging with 125 possible orientations, and note that the use of a greater number of orientations does not noticeably affect the resulting stress–strain curve.

The results are shown in Fig. 6 by the solid curves for indicated strain rates. Again, as is seen, good quantitative predictions have emerged from an experimentally supported physics-based model. Since the material-model parameters have been established through independent experiments reported by Nemat-Nasser and Li (1998), the remarkable predictive capability of the model clearly underscores the significance of experimentally supported, physics-based modeling in metal plasticity (and, in general). In this connection, it may be significant to bear in mind the experimental conditions and the measurement techniques used by Hommel and Kraft (2001) and Espinosa et al. (2004). The first authors optically measure the average macroscopic strain of the polycrystalline membrane and assume that to be the same as the local strain for all crystal orientations; this is similar to the Taylor model assumption. The stress, however, is inferred from the measured local lattice dimensional changes for a specific crystal of desired orientation. In the experiments by Espinosa and coworkers, both the strain and stress are inferred from the measured macroscopic deformations of the membrane and the corresponding applied loads. Therefore, the values of the model parameters that are based on the results of macroscopic experiments are in fact the appropriate quantities to be used for the model predictions in both cases.

6. Crystal orientation and active slip systems

As has been shown by Taylor (1934), in general, up to eight slip systems can be active in an fcc crystal, although only five of these can be independent. It can be shown that, in a

[2]This has been confirmed by Professor Espinosa in a private communication.

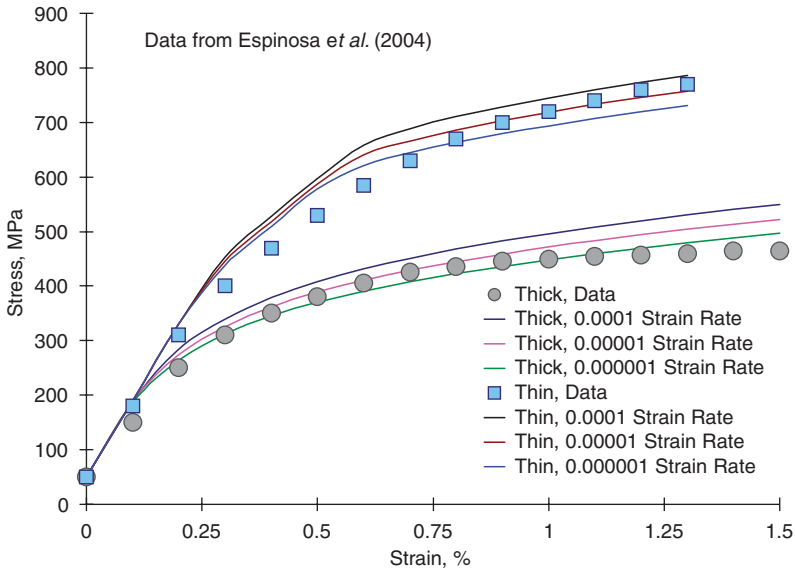

Fig. 6. Globally measured stress and strain in thin, 0.2 nm (upper data points), and in thick, 1.0 μm (lower data points), films with (1 1 1) plane parallel to the film surface, vs. measured overall macroscopic strain of a polycrystalline membranes, and the corresponding simulation results using the values of the model parameters (Table 1, second row) reported by Nemat-Nasser and Li (1998), for indicated strain rates.

fully developed plastic deformation of a crystal, either six or eight slip systems are generally active; see Nemat-Nasser (2004, Subsection 6.5.6, p. 453). Our physics-based slip model of crystal plasticity allows direct calculation of all slip rates; see Nemat-Nasser (2004, Subsection 6.5.11, p. 462). We now illustrate this considering uniaxial straining of a film in the [0 0 1]-direction, similar to the Hommel–Kraft experiment, and calculate for crystals with different orientations the equivalent stress and the corresponding slip rates at 2% overall strain. The aims here are (1) to demonstrate that even in a given polycrystal, the effective axial stress can vary by a factor of two or greater, depending on the crystal orientation even when we use the same elastic modulus for all orientations, and (2) the slip rates of all active slip systems (in fcc crystal, up to eight) can be computed.

Let the [1 0 0]-direction be normal to the plane of the film, and consider various crystals whose axes are obtained through the following rotation matrix:

$$R = \begin{bmatrix} \cos\varphi & \frac{\sqrt{2}}{2}\sin\varphi & \frac{\sqrt{2}}{2}\sin\varphi \\ -\frac{\sqrt{2}}{2}\sin\varphi & \frac{1}{2}\cos\varphi + \frac{1}{2} & \frac{1}{2}\cos\varphi - \frac{1}{2} \\ -\frac{\sqrt{2}}{2}\sin\varphi & \frac{1}{2}\cos\varphi - \frac{1}{2} & \frac{1}{2}\cos\varphi + \frac{1}{2} \end{bmatrix}, \tag{51}$$

where φ is allowed to vary from 0 to $\pi/2$, defining various orientations relative to the loading direction relative to the ([1 0 0], [0 1 0], [0 0 1]) coordinate system. If the overall deformation-rate tensor is D, then for a crystal whose orientation is defined by the angle φ, the deformation-rate tensor in that crystal's lattice coordinates would be $D' = RDR^{\mathrm{T}}$. In what follows, D is a diagonal matrix whose non-zero components are: $D_{11} = 1/\mathrm{s}$ and

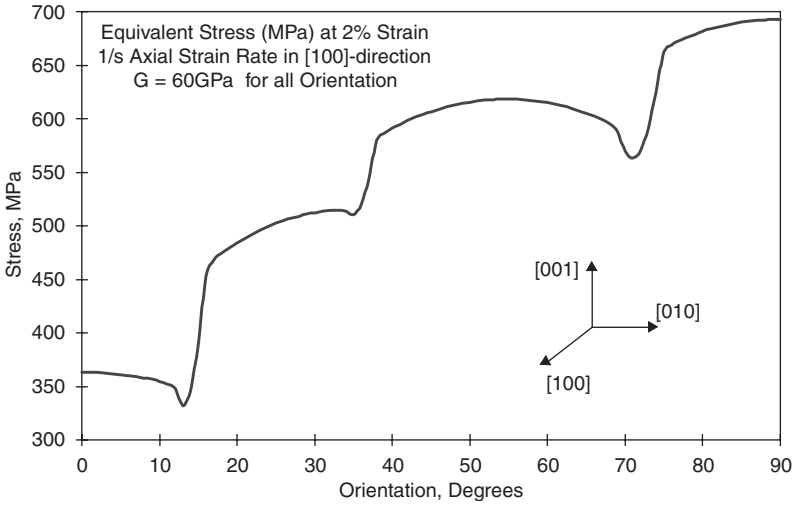

Fig. 7. Equivalent stress (axial stress) as a function of the angle φ at 2% strain, 1/s axial and -0.5/s lateral strain rates; data from Table 1 for annealed copper and $G = 60$ GPa; $\varphi = 0$ corresponds to the shown crystal coordinates.

$D_{22} = D_{33} = -0.5/\text{s}$. For the sake of illustration and in order to reduce the required computational efforts, we use the common shear modulus 60 GPa for all cases.

Fig. 7 shows the equivalent stress (axial stress) as a function of the angle φ, that is, for the same overall deformation rate defined by $D_{11} = 1/\text{s}$ and $D_{22} = D_{33} = -0.5/\text{s}$, we consider a typical crystal with lattice orientation defined by angle φ, and calculate the effective stress of that crystal. The resulting curve shows large variations in its slope as different crystal orientations are considered, suggesting that different slip systems are active in crystals of different orientations. Note that the effective axial stress has a range from about 330 to almost 700 MPA, depending on the crystal orientation, even for a common elastic modulus.

Fig. 8 gives the slip rates of all active slip systems as functions of the relative lattice orientation, φ. The slip systems numbered 3 and 11 are inactive and the systems 6 and 7 have the same slip rates, for all considered orientations in this example. For the values of φ in the range 0–13° (say, Range I), eight slip systems are active at 2% strain. For φ from 13 to 15°, the situation is dramatically different, where the slip rates of the systems 1, 2, 4, and 8 are decreasing as the orientation angle φ increases, reducing to zero at 16°, while the slip rates of systems 5 and 9 gradually increase as φ increases, being fully active for φ equal to or greater than 18°. The crystals oriented in the range of 16–34° (say, Range II) have six active slip systems, four of which are in common with the crystals in Range I. The situation is again dramatically different for crystals oriented in the range 35–37°, where two systems, 10 and 12, which are active in Range II, are inactive for φ between 37 and 69° (say, Range III), while systems 1 and 2 that are inactive in Range II, are active in Range III. Finally, for orientations in the range 69–73, the situation is quite different, and then for φ greater than, say, 74 up to 90°, eight slip systems, 1, 2, 4, 6–8, 10, and 11, are active with 4 and 8 having the same slip rates (in addition to 6 and 7).

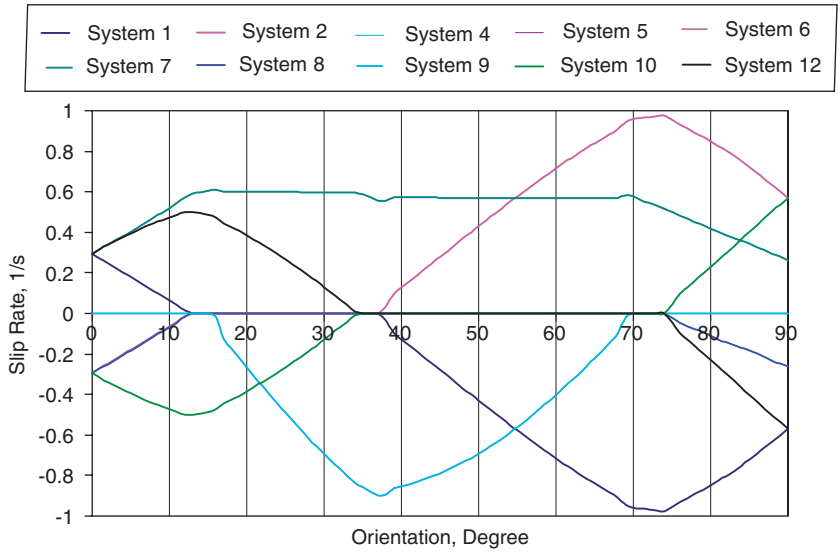

Fig. 8. Slip rates of active slip systems as functions of the crystal orientation, φ, at 2% strain, 1/s axial and -0.5 lateral overall strain rates; data from Table 1 for annealed copper; $G = 60$ Gpa.

7. Through-thickness texture effect

We now examine the effect of the mismatch of the crystal lattice orientations through the thickness of a very thin membrane, on its elastic-plastic response. For illustration, we consider a case where, on the average, the membrane is only three-crystals thick, but allow for an isotropic orientational variation over the width of the membrane. The calculations are performed using a finite-element approach, as detailed in Section 8. In what follows, we report the results of the calculation.

We use a unit cell consisting of three cubic elements, each with a specific lattice orientation, Fig. 9. The unit cell is being deformed in uniaxial straining. The overall strain rate is defined by $D_{11} = 1/\text{s}$ and $D_{22} = D_{33} = -0.5/\text{s}$, all other components of the overall deformation-rate tensor being zero; the boundary conditions are adjusted so that the top and bottom surfaces of the unit cell in Fig. 9 are traction-free, and the initially co-planar lateral surfaces of the three cubes remain co-planar as the unit cell is being uniaxially strained. The stress-deformation relation for each active slip system is the same as before, with constitutive parameters given in Table 1 for the as-received (un-annealed) case (second row in Table 1). To simplify the calculations, we assume the common shear modulus of $G = 60$ GPa and Poisson ratio of 0.34 for all orientations, although, as discussed before, the shear modulus depends on the lattice orientation. Calculations can be performed taking into account the variation in the shear modulus with lattice orientation, and this would accentuate the effect that we are seeking to illustrate, but at the cost of a considerably greater amount of computational effort. Since we are not at this point addressing any specific experimental result, for illustration the simplified calculation is considered adequate.

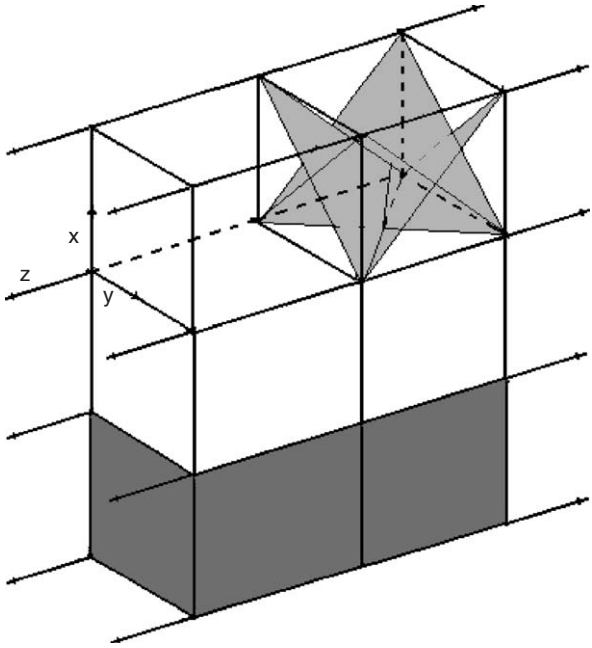

Fig. 9. The unit cell used for the finite-element modeling of the through-the-thickness lattice orientational mismatch in a very thin membrane in uniaxial straining; extended lines in the Z-direction indicate prescribed boundary velocities; in this illustration, two layers of $\langle 1\,0\,0\rangle$ texture are situated on one layer of $\langle 1\,1\,1\rangle$ texture, with the initial orientation of slip planes of the top crystal being shown.

We compare the stress–strain curves of four different cases. These are:

1. The $\langle 1\,1\,1\rangle$ texture, where the $\langle 1\,1\,1\rangle$ lattice plane of all three layers is parallel to the membrane surface.
2. The $\langle 1\,0\,0\rangle$, $\langle 1\,1\,1\rangle$, $\langle 1\,0\,0\rangle$ texture, where the middle crystal layer has the $\langle 111\rangle$ texture while the outer layers have the $\langle 1\,0\,0\rangle$ texture.
3. The $\langle 1\,1\,1\rangle$, $\langle 1\,0\,0\rangle$, $\langle 1\,0\,0\rangle$ texture, where a $\langle 1\,1\,1\rangle$ textured crystal layer is situated on two $\langle 1\,0\,0\rangle$ textured layers.
4. The $\langle 1\,0\,0\rangle$-texture, where the $\langle 1\,0\,0\rangle$ lattice plane of all three layers is parallel to the membrane surface.

For each texture, we calculate the overall effective stress of the unit cell 8^3 times, starting with a given orientation of the three lattices, and rotating the lattice orientation of each crystal by $\pi/8$ about the overall [1 0 0] axis (the overall X-axis which is normal to the membrane surface), while keeping the orientation of the lattices of the other two layers fixed. In this manner, we seek to account for the variation of the lattice orientations over the membrane's width. We then use a Taylor averaging on the resulting 8^3 values of the effective stress for each value of the effective overall strain, arriving at the stress–strain curves shown in Fig. 10.

As is seen, the response is strongly dependent on the texture of each layer, as well as on the relative position of the same layers. The membrane with one layer of the $\langle 1\,1\,1\rangle$

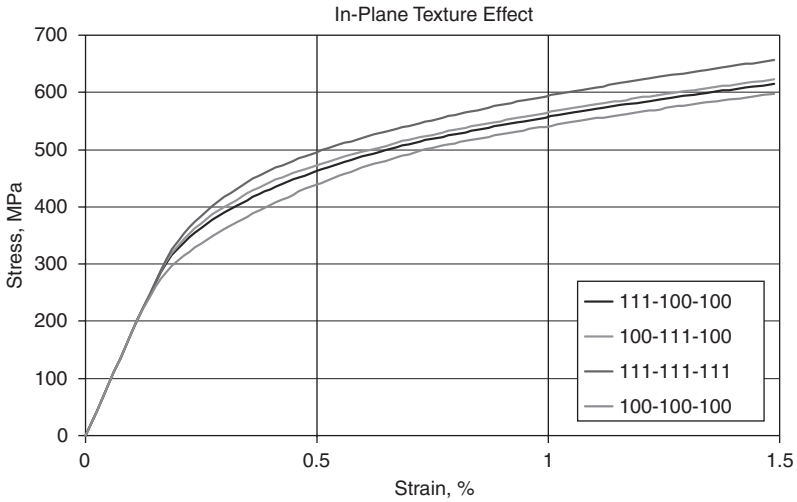

Fig. 10. Stress–strain curves for membranes of three-crystal thickness: (top curve) membrane with three layers of $\langle 1\,1\,1 \rangle$ texture; (second from top) membrane with one $\langle 1\,1\,1 \rangle$ texture crystal layer between two crystal layers of $\langle 1\,0\,0 \rangle$ texture; (third from top) membrane of $\langle 1\,1\,1 \rangle$ texture crystals situated on two layers of $\langle 1\,0\,0 \rangle$ texture; and (bottom) membrane with three layers of $\langle 100 \rangle$ texture.

texture sandwiched between two layers of the $\langle 1\,0\,0 \rangle$ texture, is stiffer than the membrane with one layer of the $\langle 1\,1\,1 \rangle$ texture over two layers of the $\langle 1\,0\,0 \rangle$ texture. Of course, the membrane with three layers of the $\langle 1\,1\,1 \rangle$ texture is the stiffest of the four considered cases, and that with the $\langle 1\,0\,0 \rangle$ texture the most compliant. Note that, in actuality, the difference between the stress–strain curves for the $\langle 1\,1\,1 \rangle$ and the $\langle 1\,0\,0 \rangle$ textures would be considerably greater if we also take into account the variation of the elastic shear modulus with the lattice orientation, i.e., say 60 GPa for the 111-direction and 20 GPa for the 100-direction, as is exemplified by the experimental results of Hommel and Kraft and their simulation presented in Fig. 5.

8. Finite-element approximation

We now outline an alternative finite-element approach that we have chosen to use for the calculations described in the preceding section. Since the unknown strain-rate tensors, D^* and D^p, are functions of the velocity field of the polycrystal, we express the strain-rate tensor components in terms of the velocity field using a standard finite-element approximation. In this modeling, all crystals of the considered polycrystalline body are approximated as isoparametric eight-node solid elements (Grandin, 1986). The resulting strain-rate tensor in each element is thus defined in terms of 24 nodal velocities,

$$\{D\} = [B]\{u\}, \tag{52}$$

where $\{u\}$ is the vector of the nodal velocities, $\{D\}$ is the vector of the components of the strain-rate tensor, and $[B]$ is a matrix that depends on the shape of the elements; the exact form of this matrix can be found in Grandin (1986).

In view of the elasto-viscoplastic nature of the constitutive model, two velocity fields are used in our calculations,

$$\{u\} = \{u_e\} + \{u_p\}. \tag{53}$$

The velocity fields $\{u_e\}$ and $\{u_p\}$ correspond to the elastic and viscoplastic deformation of the body, respectively. Strain-rate tensor D^p depends only on $\{u_p\}$, and the elastic strain-rate tensor D^* depends only on $\{u_e\}$. In general, a virtual work-rate formulation can be used to find any number of unknown parameters. The additional unknown velocity field makes the solution more cumbersome, but it considerably simplifies our numerical algorithm, because it eliminates the necessity for numerical treatment of very stiff sets of differential equations, typical in standard elastic-plastic calculations (see Nemat-Nasser, 2004, Chapter 5). The velocity field $\{u\}$ is continuous at the boundaries between finite elements. There are no continuity conditions for the velocity field $\{u_p\}$ that corresponds to the plastic deformation. To model the uniaxial tension, the boundary conditions corresponding to a prescribed uniform tensile velocity field and stress-free lateral surfaces are considered for the unit cell shown in Fig. 9.

Finite-element approximations reduce Eq. (41) to a set of non-linear equations for the unknown nodal velocities, $\{u\}$ and $\{u_p\}$. This set of equations is solved by iteration. At each iteration step, the non-linear velocity function Eq. (29) is linearized as follows:

$$\tau^{(\alpha a)}(\dot{\gamma}^{(\alpha a)}) \approx \frac{\tau^{(\alpha a)}(\dot{\gamma}_p^{(\alpha a)})}{\dot{\gamma}_p^{(\alpha a)}}\,\dot{\gamma}^{(\alpha a)}, \tag{54}$$

where the slip rates $\dot{\gamma}_p^{(\alpha a)}$ are taken from the preceding iteration step. Convergence of an iteration process of this kind has been investigated by Olevsky and Maximenko (1994). Here, the accuracy of the iteration is considered to be sufficient when the change in the value of the average stresses in the membrane from iteration to iteration in the volume of the polycrystalline body does not exceed 0.01%. Finite-element calculations have been tested by comparison against single-crystal stress–strain curves obtained by the plastic-predictor/elastic-corrector method and shown in the previous chapters of the article.

Once the velocity field in the crystals is found, the spin Ω^* is calculated according to Eq. (11), and the increment of rigid-body rotation is estimated using Eq. (9), which, from the Cayley–Hamilton theorem (Nemat-Nasser et al., 1998), becomes

$$\Delta R^* = 1 + \frac{\sin\,\omega}{\omega}\,\Omega^*\,\mathrm{d}t + \frac{1-\cos\,\omega}{\omega^2}(\Omega^*\Delta t)^2, \quad \omega^2 = -\frac{tr\left[(\Omega^*\Delta t)^2\right]}{2}, \tag{55,56}$$

The new orientation of the slip systems is then obtained from,

$$p_{t+\Delta t}^{(\alpha a)} = \Delta R^* p_t^{(\alpha a)} \Delta R^{*\mathrm{T}}. \tag{57}$$

All quantities at time t are now calculated and the iteration is repeated.

9. Conclusions

By means of illustrative examples, the sample-size effects, observed in the plastic deformation of very thin metallic membranes, are examined. Two different origins of the size effect have been addressed by numerical simulations, the orientational incompatibility of the crystals and the potential effect of surface contamination in very thin membranes.

It is shown that an increase of the yield stress with a decrease of the membrane thickness most likely is caused by the effect of orientational incompatibility of adjacent crystals and by surface hardness due to oxidation or contamination, both of which generally are insignificant when there are a sufficient number of interior crystals through the membrane thickness. A crystal plasticity model can qualitatively account for such size effects. When, in addition, a physics-based experimentally supported slip model is used, excellent quantitative results are obtained. We have demonstrated this by direct calculation, providing quantitative results, in full accord with data on thin copper membranes, using the values of the constitutive parameters that have been experimentally evaluated by Nemat-Nasser and Li (1998) for OFHC copper. *The fact that the direct application of a physics-based dislocation model of crystal plasticity*, *without any adjustment in the already published values of the involved constitutive parameters*, *accurately reproduces the results of two sets of independent experiments on thin copper films of various thicknesses*, *clearly underscores the efficacy of this general approach to material modeling.* While dislocation-based physical models of the kind presented in this work naturally involve several microscopic dislocation-based length scales, these length scales have little if any relation to the macroscopic length scales in the phenomenological gradient plasticity models. Those models include, in an ad hoc manner, the gradients of the plastic strains in their constitutive relations, thereby producing free parameters with physical dimension of length that are then used to fit data in specific cases, or are used for other purposes.

References

Balendran, B., Nemat-Nasser, S., 1993a. Double sliding model for cyclic deformation of granular materials, including dilatancy effects. J. Mech. Phys. Solids. 41 (3), 573–612.

Balendran, B., Nemat-Nasser, S., 1993b. Viscoplastic flow of planar granular materials. Mech. Mater. 16 (1–2), 1–12.

Cailletaud, G., Diard, O., Feyel, F., Forest, S., 2003. Computational crystal plasticity: from single crystal to homogenized polycrystals. Tech. Mech. 23, 130–145.

Choi, Y., Suresh, S., 2002. Size effect on the mechanical properties of thin polycrystalline metal films on substrates. Acta Mat. 50, 1881–1893.

Espinosa, H.D., Prorok, B.C., Pang, B., 2004. Plasticity size effect in free-standing submicron polycrystalline FCC films subjected to pure tension. J. Mech. Phys. Solids 52, 667–689.

Fleck, N.A., Hutchinson, J.W., 2001. A reformulation of a class of strain gradient plasticity theories. J. Mech. Phys. Solids 49, 2245–2271.

Fleck, N.A., Muller, G.M., Ashby, M.F., Hutchinson, J.W., 1994. Strain gradient plasticity: theory and experiment. Acta Metall. 42, 475–487.

Grandin, H., 1986. Fundamentals of the Finite Element Method. Macmillan, New York.

Havner, K., 1992. Finite Plastic Deformation of Crystalline Solids. Cambridge University Press, Cambridge.

Hommel, M., Kraft, O., 2001. Deformation behavior of thin copper films on deformable substrates. Acta Mater. 49, 3935–3947.

Hutchinson, J.W., 2000. Plasticity at the micron scale. Int. J. Solids Struct. 37, 225–238.

Kapoor, R., Nemat-Nasser, S., 1998. Determination of temperature rise during high strain rate deformation. Mech. Mat. 27, 1–12.

Kocks, U.F., Argon, A., Ashby, M.F., 1975. Thermodynamics and kinetics of slip. Progress in Materials Science, 19. Pergamon, New York, pp. 68–170.

Nemat-Nasser, S., Isaacs, J.B., Starrett, J.E., 1991. Hopkinson techniques for dynamic recovery experiments. Proc. R. Soc. London A 435, 371–391.

Nemat-Nasser, S., Isaacs, J., 1997. Direct measurement of isothermal flow stress of metals at elevated temperatures and high strain rates with application to Ta and Ta–W alloys. Acta Mater. 45 (3), 907–919.

Nemat-Nasser, S., 2004. Plasticity: A Treatise on the Finite Deformation of Heterogeneous Inelastic Materials. Cambridge University Press, Cambridge.

Nemat-Nasser, S., Li, S.Y., 1998. Flow stress of F.C.C. polycrystals with application to OFHC Cu. Acta Mater. 46, 565–577.

Nemat-Nasser, S., Okinaka, T., 1996. A new computational approach to crystal plasticity: fcc single crystal. Mech. Mater. 24, 43–57.

Nemat-Nasser, S., Ni, L., Okinaka, T., 1998. A constitutive model for fcc crystals with application to polycrystalline OFHC copper. Mech. Mater. 30, 325–341.

Olevsky, E., Maximenko, A., 1994. Nonstationary problems of the quasistatic theory of hardening plastic bodies. Comp. Mater. Sci. 3, 247–253.

Ono, K., 1968. Temperature dependence of dispersed barrier hardening. J. Appl. Phys. 39, 1803–1806.

Orowan, E., 1934. Zur Kristallplastizität-I, II, III. Zeit. Phys. 89, 605–613, 614–633, 634–659.

Polanyi, M., 1934. Über eine Art Gitterstörung, die eine Kristall plastisch machen konnte. Zeit Phys. 89, 660–664.

Stroh, A.N., 1953. A theoretical calculation of the strored energy in a work-hardened material. Proc. R. Soc. London B 67, 391–400.

Taylor, G.I., 1934. The mechanism of plastic deformation of crystals—I, II. Proc. R. Soc. Lond. A. 145, 362–387, 388–404.

Wu, T.Y., Bassani, J.L., Laird, C., 1991. Latent hardening in single crystals I. Theory and experiments. Proc. R. Soc. Lond. A 435, 1–19.